Available online at www.sciencedirect.com
ScienceDirect
Proceedings of the Combustion Institute 33 (2011) 743–750
Proceedings of the Combustion Institute
www.elsevier.com/locate/proci

Soot and thin-filament pyrometry using a color digital camera

Peter B. Kuhn, Bin Ma, Blair C. Connelly, Mitchell D. Smooke, Marshall B. Long *

Department of Mechanical Engineering, Yale University, New Haven, CT 06511, USA

Available online 6 August 2010

Abstract

A simple and compact temperature and soot volume fraction diagnostic technique based on ratio pyrometry has been studied. Two different consumer digital single lens reflex cameras were evaluated for use as pyrometers. The incandescence from soot and a SiC filament was imaged at the three wavelengths of each camera's color filter array (CFA). After characterization of the detector's signal response curves, temperatures were calculated by two-color ratio pyrometry using a lookup table approach. A SiC filament with known emissivity was shown to provide an absolute light intensity calibration, which further allows the soot volume fraction to be determined. Measurements were carried out on four different flames with varying levels of soot loading. The filament-derived gas temperature and soot temperature measurements have been compared with computational results and overall good agreement has been shown. Soot volume fraction measurements have been compared with previous LII results, with excellent agreement for both cameras tested.

Keywords: Optical diagnostics; Soot pyrometry; Thin-filament pyrometry

1. Introduction

Knowledge of temperatures and soot concentrations can prove valuable in understanding the processes responsible for soot production. Optical pyrometry has proven to be a practical measurement technique that can provide the temperature and concentration of soot particles in a flame by sampling the incandescence of soot that has been heated to flame temperatures [1–6]. In regions where soot is not present, gas temperatures have been inferred from pyrometry of thin filaments inserted into a flame [7–11]. Prior pyrometry methods have incorporated a variety of detection methods ranging from single photodetectors to scientific-grade imagers. Recently, Maun et al. [7] provided an overview of imaging systems used for pyrometry measurements and further showed that a consumer-grade digital camera could provide results for thin filament pyrometry (TFP). In their work, the total intensity of light was measured with the camera and correlated to thermocouple temperature measurements.

In the work described here, a color digital camera is also utilized, but the ratio of two colors is used to determine the temperature of both soot and a SiC fiber inserted into nonsooting regions

* Corresponding author. Address: Department of Mechanical Engineering, Yale University, P.O. Box 208284, New Haven, CT 06520-8284, USA. Fax: +1 203 432 6775.
E-mail address: marshall.long@yale.edu (M.B. Long).

1540-7489/$ - see front matter © 2010 The Combustion Institute. Published by Elsevier Inc. All rights reserved.
doi:10.1016/j.proci.2010.05.006

of a coflow diffusion flame. Incandescence from the soot and the fiber is imaged at the three wavelengths of the camera's color filter array (CFA) and the temperature is calculated using two-color ratio pyrometry [1–3]. It is further demonstrated that the image of the filament can provide an absolute intensity calibration, which allows calculation of the soot volume fraction.

2. Camera characterization

Over the last several years, a number of digital single lens reflex (DSLR) cameras have been introduced, with a steady increase in performance factors such as resolution, dynamic range, and sensitivity. The possibility of using these detectors for quantitative measurements is attractive from the standpoint of cost, but their suitability for such an application is not a given, since consumer digital cameras are not designed for use as scientific detectors. To establish the reliability of the cameras for quantitative work, the performance of two cameras was investigated under controlled conditions. It is important to avoid some of the built-in image processing algorithms that are appropriate for snapshots, but could invalidate the assumption that the signal can be related linearly to light intensity. Fortunately, many consumer digital cameras have the ability to record images in "raw" mode, which minimizes the internal processing of the information read from the camera chip.

Two representative cameras from recent generations of consumer DSLRs are considered here – the Nikon D70 and Nikon D90. Each offers the necessary manual user control of settings and 12-bit raw data format at a reasonable price. The D70 is based on a CCD detector (23.7 mm × 15.6 mm) with 6.1 million (effective) pixels (2014 × 3040). The D90 utilizes a CMOS sensor (23.6 mm × 15.8 mm) with 12.9 million pixels (2868 × 4352). All image enhancement options, such as sharpness, contrast, color, and saturation, were set to either "normal" or "none," as applicable, in order to ensure shot-to-shot consistency. The ISO number was set to 200 (the lowest standard setting). A white balance of "direct sunlight," was selected, but this setting simply specifies a set of color balance multipliers that were not used in processing the image data.

Files were saved in the camera's "NEF" format, which is a 12-bit lossless compressed raw format. Although used by many camera manufacturers as a designation for unprocessed images, raw is not a standardized format (unlike TIF, JPG, etc.). Consequently, some careful examination of the resulting image is necessary to ensure consistent reconstruction of the underlying intensity data. To facilitate a more transparent analysis, the open-source image-processing software OMA [12] was used to capture images, transfer them to the computer, and perform subsequent processing. Decoding of the Nikon-specific data format is done within the OMA program using a publicly available software library [13].

It was verified that the signal detected by the D70 in all three channels decreased linearly with attenuation and increased linearly with exposure, up to the point where the channels saturate (see Supplementary data). The signal is seen to increase linearly with increasing exposure time up to the point of saturation. A line fit to the data in the linear region results in an R^2 value that is greater than 0.999 for all three color channels. Within the linear region, the signal ratio between the different color channels exhibits a standard deviation of 1% across all data triplets. Similar results were obtained using the D90. In the following, the cameras were operated in this linear regime.

The pyrometry experiments described below require characterization of the spectral response of the detector/CFA system, which is not available from the manufacturer. To provide this data, the spectrum of an illumination source was imaged onto a ground glass diffuser (DG20-1500) using an imaging spectrograph (Jobin Yvon CP200), with a 200 groove/mm grating and a 0.05 mm entrance slit. The dispersed spectrum was imaged onto each digital camera through a Nikkor 50 mm f/1.4 lens. The data were separated into three images corresponding to the red, green, and blue (RGB) channels of the CFA. Spectral scaling was determined by imaging the 404.7, 435.8, 546 and 578.2 nm lines from a mercury vapor lamp. Normalization for the spectrum of the illumination source and optical throughput of the spectrograph was obtained by imaging the spectrum with a scientific camera (Cooke Sensicam with SuperVGA sensor), whose typical spectral response has been tabulated by the manufacturer. The illumination source (Fiber-Lite Series 180) was observed to be stable, giving no noticeable variation over time. All components used were fixed in position, with the lens aperture set to f/2. Only the camera body was changed for different trials. The spectral response of the Nikon D70 and D90 were measured with a BG-7 filter in the setup in order to provide better balance between the red, green, and blue intensities that are encountered in the pyrometry experiments. Figure 1 shows the measured spectral response for the D70 and D90. The RGB channels from both cameras show similar characteristics – significant spectral overlap between channels, with a shape not accurately represented by a single Gaussian curve.

To further characterize the detectors, an independent blackbody calibration was performed. Both the D70 and D90 recorded images of a blackbody source (Pegasus R, Model 970) at temperatures ranging from 800 to 1200 °C, in increments of 50 °C. Data from these calibrations are presented in the next section.

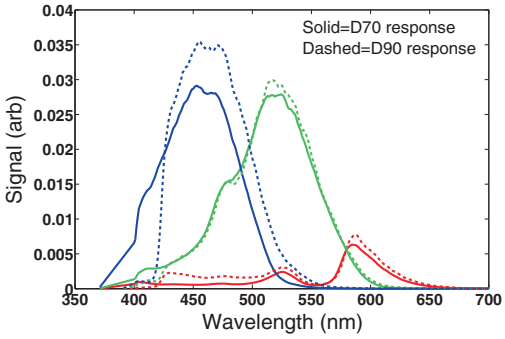

Fig. 1. Nikon D70 and D90 CFA response curves, coupled with a BG-7 filter, for the blue, green and red filters (from left to right). (For interpretation of the references to color in this figure legend, the reader is referred to the web version of this article.)

3. Ratio pyrometry background

The intensity of radiation emitted by a material at wavelength λ, is dependent on the material's emissivity $\varepsilon(\lambda)$ and the temperature T according to Planck's law:

$$I(\lambda, T) = \varepsilon(\lambda)\frac{2\pi hc^2}{\lambda^5(e^{hc/\lambda kT} - 1)} \quad (1)$$

where c is the speed of light, h is Planck's constant, and k is the Boltzmann constant. The measured signal, S_F, detected through a color filter in a time interval τ is the intensity of radiation integrated over the detection wavelengths:

$$S_F = (2\pi hc^2)\tau \int_{\lambda_1}^{\lambda_2} \frac{\varepsilon(\lambda)\eta(\lambda)}{\lambda^5(e^{hc/\lambda kT} - 1)} d\lambda \quad (2)$$

where $\eta(\lambda)$ accounts for the efficiency of the detector, the combined lens and filter transmittance, as well as a geometric factor. λ_1 and λ_2 are the low and high limits of the filter bandwidth, which are approximately 400 and 700 nm. In conventional ratio pyrometry applications, the filter bandwidths at two central wavelengths are selected to be narrow compared with the spacing between two filters. This approach, outlined by Levendis et al. [1], takes a signal ratio at two spectral bands, and uses the finite filter widths and mean multipliers for each filter at the central wavelengths to simplify Eq. (2). The result is an implicit temperature equation that can be solved iteratively for a measured signal ratio using a calibration that characterizes the detection system. In this approach, the filters are described only by a single mean wavelength and a spectral width.

The assumption of narrowband detection filters made to derive the implicit temperature equation, however, is not valid for the CFAs on the color digital cameras being considered here (see Fig. 1). Clearly the filter functions are broad and relatively complex and thus the Planck function varies significantly within each of the three spectral detection windows of the CFA. In previous work [14–16] it was shown that the effect of the variation in the Planck function over a broad spectral window could be overcome by calculating a new effective filter wavelength for each iteration of the temperature equation. Alternatively, it is possible to evaluate Eq. (2) without making approximations of the filter profiles. In this approach, the signal ratio is derived directly from Eq. (2) to be

$$\frac{S_{F_1}}{S_{F_2}} = \frac{\int \eta_{F_1}(\lambda)\frac{\varepsilon(\lambda)}{\lambda^5}[\exp(hc/\lambda kT) - 1]^{-1} d\lambda}{\int \eta_{F_2}(\lambda)\frac{\varepsilon(\lambda)}{\lambda^5}[\exp(hc/\lambda kT) - 1]^{-1} d\lambda} \quad (3)$$

for filters F_1 and F_2, where $\eta_{F_1}(\lambda)$ and $\eta_{F_2}(\lambda)$ are the respective transmission efficiencies for each color channel as a function of wavelength. The ratio can be calculated by evaluating the integrals in Eq. (3) numerically based on the characteristics of the detection system for a range of input temperatures. Assuming the signal ratio is single valued over the temperature range of interest, this lookup table can be used to determine temperatures based on the ratio of two colors. A camera with three separate filters will provide three ratios, all of which can be used in determining the most likely final temperature.

Figure 2 shows three signal ratios as a function of temperature for the D90 camera. Solid lines correspond to the ratios calculated for a blackbody source using Eq. (3) and the measured camera response shown in Fig. 1. Individual dots show the results of the blackbody calibration, and dashed lines show the expected signal ratio for soot. The agreement between the measured blackbody ratios and the ratios calculated from the measured spectral curves are improved by small modifications (<5%) to the RGB scaling parameters and these are included in the ratios shown in Fig. 2 as well as in the response shown in Fig. 1. To generate the soot lookup table, the emissivity of soot is assumed to vary with

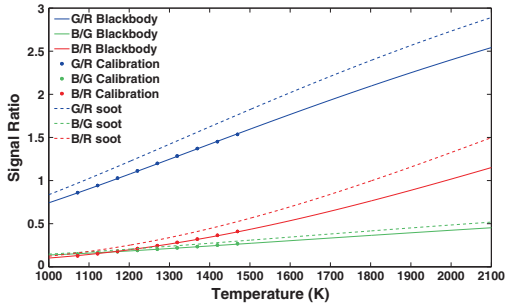

Fig. 2. D90 signal ratios vs. temperature lookup table for a blackbody or gray body (solid lines) and soot (dashed lines), validated by an independent blackbody calibration. Individual dots show the results of the blackbody calibration.

$\lambda^{-1.38}$. This is based on the wavelength dependence of the refractive index measured by Chang and Charalampopoulos [17] together with the expression for emissivity as a function of refractive index from Ref. [2]. As the emissivity of the SiC fiber does not vary with wavelength in the visible region of the spectrum ($\varepsilon = 0.88$) [7], the emissivity terms in Eq. (3) cancel, and the blackbody lookup table can be used. A similar set of lookup tables was generated for the D70 and is shown in the Supplementary data.

4. Thin filament temperature measurement

Following the detector characterization, data were taken in sooting, axisymmetric, laminar ethylene diffusion flames, with varying degrees of fuel dilution by nitrogen. The burner consists of a 0.4 cm inner diameter vertical tube, surrounded by a 7.4 cm coflow. Flames with different fuel mixtures were studied with ethylene concentrations of 32%, 40%, 60%, and 80%, by volume. For all flames, the fuel velocity at the burner surface had a parabolic profile and the air coflow was plug flow, both with an average velocity of 35 cm/s. This configuration has been studied previously as part of an ongoing experimental and computational collaboration [18]. A description of the computations used here for the temperature and soot volume fraction comparisons is included in the Supplementary data.

The flames were imaged through the BG-7 filter at f/16 with an 85 mm focal length lens, offset from the camera body with an extension ring. The lens configuration was chosen to approximate parallel ray collection, which is a necessary assumption for the Abel inversion required for the soot pyrometry described in the next section [19,20]. The filament, with a length of ~7 cm and diameter of 15 μm as measured with an optical microscope, was attached with tape to metal rods and placed horizontally in the flame. Measurements were made at 30.0, 39.0, 59.6 and 83.9 mm above the center of the burner for the 32%, 40%, 60% and 80% flames, respectively. These locations were well beyond the sooty region to avoid interference from soot emission.

For each filament temperature measurement, two NEF images, with and without the filament above the flame, were obtained. The one without the filament served as background and was subtracted pixel by pixel. With a perfect imaging system, the image of the fiber on the detector would be smaller than the width of one pixel (by factors

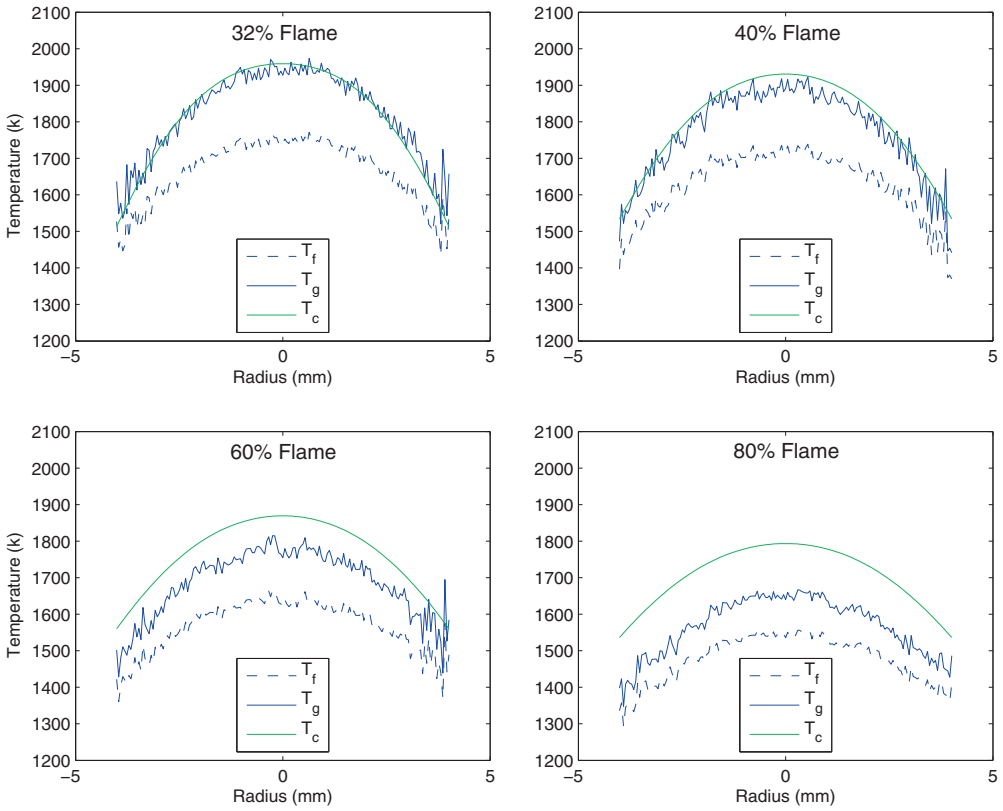

Fig. 3. Filament temperature T_f, filament-derived gas temperature T_g (both measured with the D90) and calculated gas temperature T_c from four nitrogen-diluted ethylene flames.

of 4.4 and 3.2 for the D70 and D90, respectively, after 2 × 2 binning) but aberrations in the imaging system resulted in the fiber image being spread over several pixels. A region surrounding the filament is selected to include all RGB pixels containing filament radiation and the intensities are integrated along the axial direction in this region. Dividing the RGB integrated intensities by each other yielded three ratios, and three consistent temperatures were obtained from the ratios by applying the appropriate blackbody lookup table (Fig. 2). The maximum variation of the temperatures obtained from the three ratios is ~20 K, while the average temperature is almost the same with the temperature lookup by the B/R ratio, with a maximum difference around 3 K. Figure 3 shows the filament temperatures above each of the four flames as measured by the D90 camera (in all the following results, the D70 measurements are included in the Supplementary data). The fluctuations along the profile come from the imperfection of the filament and variation of pixels. Because of the rapid drop-off in intensity at lower temperatures, filament temperatures lower than ~1400 K became dominated by noise. It should be noted that when a new filament was positioned above the flame, the RGB intensity and derived temperatures were not stable for several minutes. After aging for ~3 min, the filament temperatures and RGB signals reach a stable state.

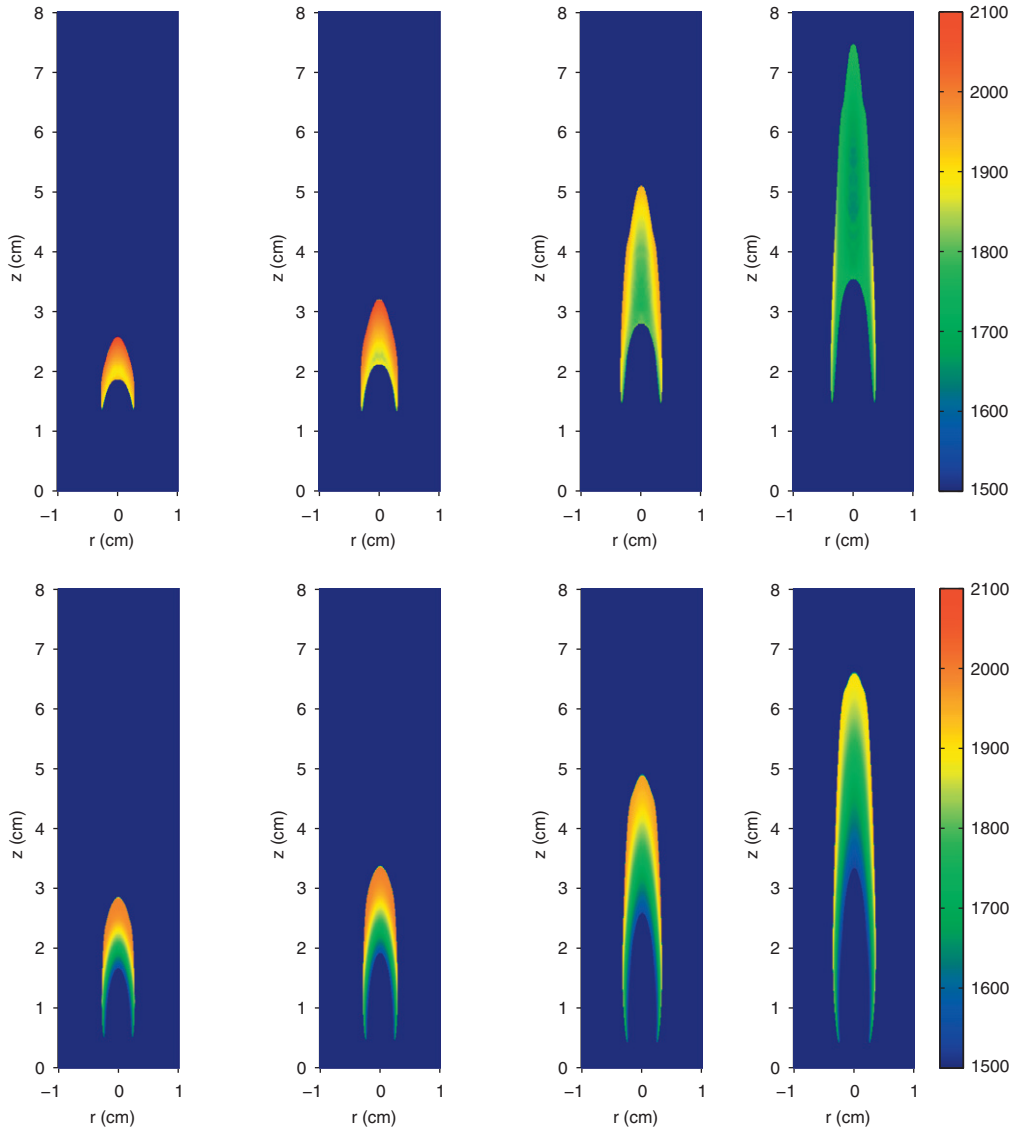

Fig. 4. Measured (top) and calculated (bottom) soot temperatures from four nitrogen-diluted ethylene flames with fuel concentrations (from left to right) of 32%, 40%, 60% and 80% C_2H_4.

The filament is heated by convective heat transfer from the surrounding hot gases and cooled by radiation transfer with the ambient environment and axial heat conduction along the filament. Therefore the filament temperature is always lower than the gas phase temperature and a correction process is needed to obtain gas temperature. The corrections are dependent on gas properties, velocity, composition, and temperature. The computations for the four N_2 diluted flames showed that N_2 occupies more than 70% volume downstream at the filament position. Therefore, gas properties used here can be based on pure N_2, for simplicity, without losing too much accuracy. The correction procedure followed the analysis of Maun et al. [7] with details given in the Supplementary data.

As shown in Fig. 3, T_f is the filament temperature, T_g is the derived gas phase temperature while T_c is the computational result. The derived gas temperature is in good agreement with the computational results for the 32% and 40% flames. For the higher fuel concentration flames, the computed temperature is seen to be higher than the measured temperatures. This difference may be attributed to less radiation loss in the computations, since the computational results predict a lower soot volume fraction than is measured.

5. Soot temperature and volume fraction in four sooting laminar flames

Soot temperature measurements were performed in the same setup as the filament temperature measurement. Each flame image was separated into three RGB images and then converted to radial profiles using an Abel inversion. Prior to the Abel inversion, the image of the full flame must be divided into

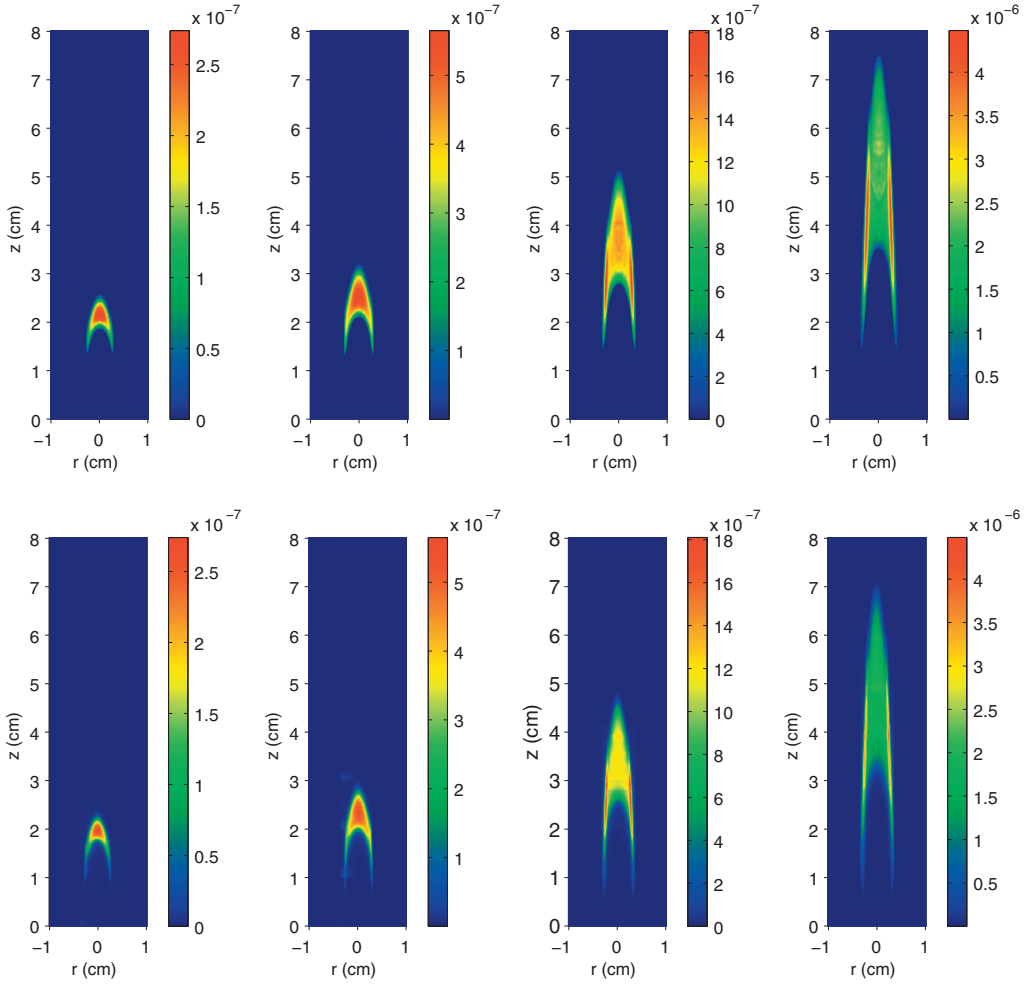

Fig. 5. Soot volume fraction measured using pyrometry (top) and LII (bottom) from four nitrogen-diluted ethylene flames with fuel concentrations (from left to right) of 32%, 40%, 60% and 80% C_2H_4.

a half image, with the symmetry axis on one side of the half image. Best results were obtained by considering each radial slice of the image (i.e., one row of pixels), finding the centroid of the row, and folding the intensities about that centroid. This makes use of both halves of the image, resulting in less noise in the final Abel-inverted profile, and eliminates any need for manual cropping of the image. Dividing the radial profiles by each other to determine the measured signal ratios and applying the soot lookup table gives three soot temperature profiles, with a maximum variation of ~30 K. The final temperature is an average of the three. Figure 4 (top) shows the measured soot temperatures from each of the flames obtained with the D90. As might be expected, the peak temperature decreases as the fuel concentration increases, due to increased soot loading and resultant radiative heat loss. Since soot pyrometry can only measure temperature where soot is present, the calculated temperature profiles shown in Fig. 4 (bottom) have been cropped to show only those regions where soot was calculated to be nonzero. While the computational model gives a somewhat different prediction of the sooting region, (which in turn results in a different shape of the cropped temperature profile) the same general trends are seen in both measurement and computation, with peak temperatures decreasing as the soot loading increases.

Once the soot temperature is known, the soot volume fraction, f_v, can be determined if an absolute intensity calibration is available for the specific optical configuration used. Following the formulation of Cignoli et al. [3] this can be expressed as

$$f_v = -\frac{\lambda_S}{K_{ext}L}\ln\left\{1-\varepsilon_L(\lambda,T_L)\frac{\tau_S}{\tau_L}\frac{S_{S\lambda}}{S_{L\lambda}} \times \exp\left[-\frac{hc}{k\lambda_S}\left(\frac{1}{T_L}-\frac{1}{T_S}\right)\right]\right\} \quad (4)$$

where λ_S is the effective filter wavelength at the soot temperature, K_{ext} is the dimensionless extinction coefficient, L is the absorption length (the dimension of one binned pixel), $\varepsilon(\lambda, T_L)$ is the emissivity of the calibration source, and τ, S_λ, T are detector parameters, signal intensity and temperature, respectively, with subscripts L and S corresponding to the calibrated light source and soot, respectively. K_{ext} was taken as 8.6 here, which is consistent with values given by Krishnan et al. [21], and matches the value used in the LII experiment that the soot volume fraction results are compared against [18]. The effective filter wavelength, λ_S, is the wavelength at the maximum value of the product of the camera filter response (see Fig. 1) and the Planck blackbody intensity evaluated at the particular soot temperature.

A blackbody calibration source or other calibrated light source can be used for calibration, as long as the optical configuration is not changed. A more convenient source of absolute intensity calibration, however, is available from the image of the filament discussed above. As long as the emissivity is known, this measurement provides a temperature (higher than that available from common blackbody sources) and an absolute RGB light intensity correlation. This has the advantage of being simple to implement, since the filament and soot measurements are performed in the same experimental configurations and the geometric factors therefore cancel. The ratio of optical parameters $\frac{\tau_S}{\tau_L}$ simply accounts for any difference in exposure times and the ratio of the length imaged onto a pixel to the filament diameter.

Figure 5 (top) shows the soot volume fraction measurements obtained in the four flames using the D90 and Fig. 5 (bottom) shows the soot volume fraction measured in the same flames using laser-induced incandescence (LII) and reported previously [18]. Agreement between the two measurement techniques is very good. It should be noted that, as with the LII results shown in Fig. 5, self-absorption is not considered. For the most highly sooting flames, this could affect the results. Incorporating the absorption into the algorithm could help improve the measurement accuracy for flames with higher soot loading. However, this approach is more mathematically complicated and is beyond the scope of this work.

6. Conclusions

Two consumer DSLRs, (one based on a CCD detector, the other with a CMOS sensor) have been characterized and were found to work well for ratio pyrometry of SiC fibers and soot. The spectral response of each detector was characterized, which allows the generation of lookup tables relating the three color ratios from the detector's RGB filters to the temperature of the fiber or soot. Use of a BG-7 color glass filter equalized the intensity in the three channels. Four C_2H_4 flames with varying levels of N_2 dilution were studied and results for the temperature obtained with the two detectors showed good agreement with each other as well as reasonable agreement with recent calculations. The SiC fiber image was shown to be useful as an absolute intensity calibration, which then allows the determination of the soot volume fraction from the ratio pyrometry measurements. Results from both detectors were in excellent agreement with those obtained in previous studies using LII.

Acknowledgements

The research was supported by the DOE Office of Basic Energy Sciences (Dr. Wade Sisk, contract monitor), the National Science Foundation (Dr. Phil Westmoreland, contract monitor), NASA

(Dr. Dennis Stocker, contract monitor) and the AFOSR (Dr. Fariba Fahroo, contract monitor) under contracts DE-FG02-88ER13966, CTS-0328296, NNC04AA03A, and AFOSR FA9550-06-1-0164, respectively.

Appendix A. Supplementary data

Supplementary data associated with this article can be found, in the online version, at doi:10.1016/j.proci.2010.05.006.

References

[1] Y.A. Levendis, K.R. Estrada, H.C. Hottel, *Review of Scientific Instruments* 63 (7) (1992) 3608–3622.
[2] S. De Iuliis, M. Barbini, S. Benecchi, F. Cignoli, G. Zizak, *Combustion and Flame* 115 (1–2) (1998) 253–261.
[3] F. Cignoli, S. De Iuliis, V. Manta, G. Zizak, *Applied Optics* 40 (30) (2001) 5370–5378.
[4] C. Beatrice, C. Bertoli, N.C. Cirillo, N.D. Giacomo, S.D. Stasio, *Combustion Science and Technology* 110 (1) (1995) 321–339.
[5] D.R. Snelling, K.A. Thomson, G.J. Smallwood, O.L. Gulder, E.J. Weckman, R.A. Fraser, *AIAA Journal* 40 (9) (2002) 1789–1795.
[6] T. Panagiotou, Y. Levendis, M. Delichatsios, *Combustion and Flame* 104 (3) (1996) 272–287.
[7] J.D. Maun, P.B. Sunderland, D.L. Urban, *Applied Optics* 46 (4) (2007) 483–488.
[8] P. Struk, D. Dietrich, R. Valentine, I. Feier, *in: 41st Aerospace Sciences Meeting and Exhibit*, AIAA, Reno, Nevada, 2003.
[9] V. Vilimpoc, L.P. Goss, *Proceedings of the Combustion Institute* 22 (1) (1989) 1907–1914.
[10] W.M. Pitts, *Proceedings of the Combustion Institute* 26 (1996) 1171–1179.
[11] W.M. Pitts, K.C. Smyth, D.A. Everest, *Proceedings of the Combustion Institute* 27 (1) (1998) 563–569.
[12] P.A.M. Kalt, M.B. Long, OMA – Image processing for Mac OS X. www.oma-x.org (1/2010).
[13] D. Coffin, http://www.cybercom.net/~dcoffin/dcraw/ (1/2010).
[14] U. Anselmitamburini, G. Campari, G. Spinolo, P. Lupotto, *Review of Scientific Instruments* 66 (10) (1995) 5006–5014.
[15] M.B. Boslough, T.J. Ahrens, *Review of Scientific Instruments* 60 (12) (1989) 3711–3716.
[16] B.C. Connelly, S.A. Kaiser, M.D. Smooke, M.B. Long, Proceedings of the Joint Meeting of the U.S. Sections of the Combustion Institute, Drexel University, Philadelphia, PA, March 2005.
[17] H. Chang, T.T. Charalampopoulos, *Proceedings of the Royal Society of London Series A-Mathematical Physical and Engineering Sciences* 430 (1880) 577–591.
[18] M.D. Smooke, M.B. Long, B.C. Connelly, M.B. Colket, R.J. Hall, *Combustion and Flame* 143 (4) (2005) 613–628.
[19] C.J. Dasch, *Applied Optics* 31 (8) (1992) 1146–1152.
[20] K.T. Walsh, J. Fielding, M.B. Long, *Optics Letters* 25 (7) (2000) 457–459.
[21] S.S. Krishnan, K.-C. Lin, G.M. Faeth, *Journal of Heat Transfer* 122 (3) (2000) 517–524.